Stability study of a constant-volume thin film flow

J. M. Gomba,* J. Diez,† R. Gratton, and A. G. González‡
Instituto de Fìsica Arroyo Seco, Universidad Nacional del Centro de la Provincia de Buenos Aires, Pinto 399, 7000, Tandil, Argentina

L. Kondic§
Department of Mathematical Sciences and Center for Applied Mathematics and Statistics, New Jersey Institute of Technology, Newark, New Jersey 07102, USA

(Received 13 June 2007; published 9 October 2007)

We study the stability of a constant volume of fluid spreading down an incline. In contrast to the commonly considered flow characterized by constant fluid flux, in the present problem the base flow is time dependent. We present a method to carry out consistently linear stability analysis, based on simultaneously solving the time evolution of the base flow and of the perturbations. The analysis is performed numerically by using a finite-difference method supplemented with an integral method developed here. The computations show that, after a short transient stage, imposed perturbations travel with the same velocity as the leading contact line. The spectral analysis of the modes evolution shows that their growth rates are, in general, time dependent. The wavelength of maximum amplitude, λ_{max}, decreases with time until it reaches an asymptotic value which is in good agreement with experimental results. We also explore the dependence of λ_{max} on the cross sectional fluid area A, and on the inclination angle α of the substrate. For considered small A's, corresponding to small Bond numbers, we find that the dependence of λ_{max} on A is in good agreement with experimental data. This dependence differs significantly from the one observed for the films characterized by much larger A's and Bond numbers. We also predict the dependence of λ_{max} on the inclination angle α.

DOI: 10.1103/PhysRevE.76.046308 PACS number(s): 47.20.−k, 68.15.+e, 47.15.Fe

I. INTRODUCTION

The dynamics of thin film flows is a key feature in numerous applications [1–3]. In particular, there is an increasing interest in understanding flows in microscopic devices designed to propel and mix small volumes of liquids. Micrometric ducts, pumps, turbines, and valves are all examples of such small devices involving flows of liquids and gases [4,5]. Even though there has been rapid progress in both manufacture and development of microelectromechanic devices (MEMS), knowledge of the physics at these small scales has advanced at a much slower pace [6,7]. For instance, one important issue, which still needs further research, is the dynamics of the contact line [8–11]. In some scenarios, the moving front becomes unstable and develops a fingerlike or sawtooth pattern, depending on the wetting conditions and/or on the inclination angle of the substrate [12–14]. Moreover, addition of surfactants may lead to complicated patterns which include the growth of dendritic structures [15–17].

The contact line instability is present in many flow configurations, such as spin coating and thermocapillary driven spreadings. In the first case, the front is unstable under azimuthal perturbations [18–22], the centrifugal force being the destabilizing agent. In the second case, it is found that the instability appears for inclination angles greater than a critical one when a temperature gradient is imposed on an inclined substrate [23–29].

Here, we concentrate on another example of the contact line instability, that of gravity driven flows on an inclined solid surface. Experimentally, and in applications, the relevant configuration is the one of a *constant volume* (CV) of fluid flowing down a plane [12,13,30–32]. The theoretical and computational models, however, are often based on a conceptually simpler *constant flux* (CF) flow, in which the film thickness is kept constant far behind the contact line [33–35]. The boundary conditions appropriate for CF flow allow one to reduce the partial differential equation governing the base flow to a time-independent ordinary differential equation for the film thickness in a moving reference frame. However, the base state of CV flow is time dependent, and computations and models based on time-independent assumption necessarily involve approximations whose validity is difficult to verify. In this work, we avoid this approach altogether, and consistently compute evolution of the perturbations superimposed on the time-dependent base state.

After the pioneer work on the instability of the contact line in the CV flow carried out by Huppert [12], other authors have studied this problem. Silvi and Dussan [30] analyze the effects of the contact angle on the ability of the fluid to coat the surface. For small contact angles, they observe that the front line adopts a fingering pattern so that the fluid eventually wets all of the surface. On the other hand, for large contact angles the troughs (zone between fingers) stop and the fluid spreads only along the fingers, so that the surface is not completely covered. Jerret and de Bruyn [31] monitor the dependence of the average wavelength (the mean distance between fingers) $\bar{\lambda}$ on the inclination angle of the substrate, α. They find that $\bar{\lambda} \propto (\sin \alpha)^{-0.41}$, with an exponent slightly larger in absolute value than the one predicted by Huppert [12], which was $-1/3$. Huppert also obtains the

*jgomba@exa.unicen.edu.ar
†http://www.exa.unicen.edu.ar/~jdiez
‡http://www.exa.unicen.edu.ar/~aggonzal
§http://www.njit.edu/~kondic

relationship between $\bar{\lambda}$ and the cross sectional area A and finds that $\bar{\lambda} \propto A^{1/6}$. We note that in all those works, the volumes of fluid are relatively large with typical cross sectional area $A > 1$ cm^2, and the typical fluid thickness h_c much larger than the capillary length a, giving large Bond numbers $B = (h_c/a)^2 \gg 1$.

In two previous works [36,37], we focus on gravity driven flow down a vertical plane, $\alpha = 90°$, for small fluid volumes characterized by $A \ll 1$ cm^2 and correspondingly small $B \ll 1$. In Ref. [36] we develop an heuristic model to account for the contact line instability of CV flow by using the dispersion relation given by the linear stability analysis of the CF flow. The growth rates of the dominant modes computed within this model are in very good agreement with those obtained in the experiments. In [37] we show that considered CV flows are characterized by a dimensionless parameter $R \propto w_0^4 \sin \alpha/(Aa^2)$, where w_0 is the initial film width in the downstream direction. In particular, for $\alpha = 90°$ we find that the wavelength of the mode of maximum amplitude λ_{max} is proportional to $w_0 R^{-0.27 \pm 0.022}$, also in agreement with the exponent predicted based on the dimensional analysis [38] for the flow down a vertical plane, i.e., $\lambda_{max} \propto A^{1/4}$. One obvious consequence of the dependence of λ_{max} on R is that B is not the main parameter which determines the emerging wavelengths, since by changing initial fluid configuration through modifying w_0, a given A could be obtained for multiple B's. However, B is a relevant parameter in determining the manner of spreading, since for large B's, the fluid front propagates mainly via rolling motion of the fluid front, like a caterpillar [39,40]. Only when the typical film thickness becomes of the order of the capillary length, the shape of the front region changes from caterpillar to wedge [40]. Consequently, the dynamics is qualitatively different for small and large B's.

In this paper, we concentrate on the flows characterized by small B's, and correspondingly, by small fluid A's so to be able to compare directly to the results of the experiments [36,37]. Furthermore, we explore how the emerging wavelengths depend on A and α, motivated particularly by the fact that current results exist only for $\alpha = 90°$. The analysis is carried out by studying the evolution of small perturbations of a CV flow within the framework of a linear stability analysis. We numerically solve the linear equation that governs their amplitudes, together with the nonlinear evolution equation governing the base flow, $h_0(x,t)$. In Sec. II we present the model used to simulate the evolution of both the base flow and the perturbations. The main difficulty in calculating perturbation amplitudes is related with the accuracy needed in the evaluation of the coefficients of the linear equation. Since these coefficients involve computing fourth order derivatives of $h_0(x,t)$, a standard discretization method requires rather small grid size, in particular, in the contact line region. In order to increase accuracy, we develop an integral method which allows one to carry out computations on more coarse grids. This method is described in Sec. III, where we also validate our numerical code by solving the CF flow. These computations are carried out in the laboratory frame and compared with the results obtained in a moving frame, where the problem is time independent. The analysis in the moving frame is presented in the Appendix. The CV flow is studied in Sec. IV, where we describe the spatial and temporal evolution of the perturbations. Finally, we compare the numerical and experimental results, and investigate the influence of A and α on the wavelength of the most unstable mode. For the purpose of simplified comparison with experiments, we mostly use the (dimensional) value of A to parametrize our results. More discussion regarding relevant nondimensional parameters describing the flow can be found in Ref. [37].

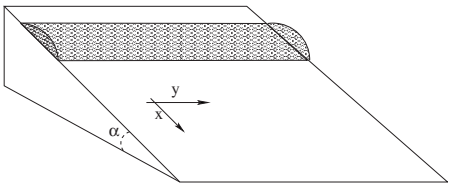

FIG. 1. Scheme of the inclined plane and coordinates axes.

II. BASIC EQUATIONS

We study the stability of thin liquid films under the lubrication approximation, therefore assuming negligible Reynolds number and small free surface slopes. A major hindrance in the development of the theory for film flows is the incomplete knowledge of the physics at the contact line. A moving contact line coupled with a no-slip boundary condition leads to a multivalued fluid velocity there. As a consequence, both the viscous dissipation rate and the shear stress diverge as fluid thickness $h \to 0$ [8,41]. We overcome this singularity by including a microscopic precursor film (of thickness h_f) ahead of the apparent contact line [42,43].

For a completely wetting fluid spreading down an inclined plane (see Fig. 1) under the action of gravity g, the governing equation for $h(x,y,t)$ is (see, e.g., Ref. [33])

$$h_t + \nabla \cdot (h^3 \nabla (\nabla^2 h)) - G_\perp \nabla \cdot (h^3 \nabla h) + G_\parallel (h^3)_x - u \nabla h = 0, \tag{1}$$

where t is time, $\nabla \equiv (\partial/\partial x, \partial/\partial y)$, and (x,y) are in-plane coordinates. The subscripts x and t in Eq. (1) stand for $\partial/\partial x$ and $\partial/\partial t$, respectively. This equation is formulated in a reference frame translating with constant velocity u; $u = 0$ corresponds to the laboratory frame. All variables are dimensionless, and we denote the scale for h as h_c, for x and y as x_c, and for t as t_c. The dimensionless parameters $G_\perp$ and $G_\parallel$ are consequently given by

$$G_\perp = \frac{x_c^2}{a^2} \cos \alpha, \quad G_\parallel = \frac{x_c^3}{h_c a^2} \sin \alpha, \tag{2}$$

where α is the inclination angle of the substrate, $a = \sqrt{\gamma/(\rho g)}$ is the capillary length, γ is the surface tension, and ρ is the fluid density. The time scale t_c is defined as

$$t_c = \frac{3\mu}{\gamma} \frac{x_c^4}{h_c^3}, \tag{3}$$

where μ is fluid viscosity.

Let us consider the y-independent solution of Eq. (1), $h_0(x,t)$, which describes the spreading of a fluid down an incline. It satisfies

$$h_{0,t} + (h_0^3 h_{0,xxx})_x - G_\perp (h_0^3 h_{0,x})_x + G_\parallel (h_0^3)_x - u h_{0,x} = 0. \quad (4)$$

In order to study the linear stability of this film with respect to perturbations in the transverse direction y we write

$$h(x,y,t) = h_0(x,t) + \epsilon g(x,t;\lambda)\exp(iqy), \quad (5)$$

where ϵ is a small parameter, $g(x,t;\lambda)$ is the amplitude of the perturbation, $q=2\pi/\lambda$ is the wave number, and λ is the wavelength. By replacing Eq. (5) into Eq. (1), we obtain to $O(\epsilon)$ the linear equation for $g(x,t;\lambda)$,

$$g_t + c_4(x,t)g_{xxxx} + c_3(x,t)g_{xxx} + c_2(x,t)g_{xx} + c_1(x,t)g_x + c_0(x,t)g = 0, \quad (6)$$

where the coefficients are defined by

$$c_4(x,t) = h_0^3,$$

$$c_3(x,t) = 3h_0^2 h_{0,x},$$

$$c_2(x,t) = -(G_\perp + 2q^2)h_0^3,$$

$$c_1(x,t) = 3h_0^2[G_\parallel - (q^2 + 2G_\perp)h_{0,x} + h_{0,xxx}] - u,$$

$$c_0(x,t) = h_0[q^2(q^2 + G_\perp)h_0^2 + 6h_{0,x}(G_\parallel - G_\perp h_{0,x} + h_{0,xxx}) + h_0(-3G_\perp h_{0,xx} + 3h_{0,xxxx})]. \quad (7)$$

In order to avoid calculating high order derivatives of h_0, it is convenient to rewrite the coefficients $c_0(x,t)$ and $c_1(x,t)$ in terms of the space- and time-dependent fluid velocity of the base solution in the laboratory frame $v(x,t)$. In fact, Eq. (4) can be written more compactly in conservative form

$$h_{0,t} + [h_0(v(x,t) - u)]_x = 0, \quad (8)$$

where

$$v(x,t) = h_0^2(h_{0,xxx} - G_\perp h_{0,x} + G_\parallel). \quad (9)$$

After some algebra, the coefficients $c_i(x,t)$ can be written as (c_2–c_4 are repeated here for later reference)

$$c_4(x,t) = h_0^3,$$

$$c_3(x,t) = 3h_0^2 h_{0,x},$$

$$c_2(x,t) = -(G_\perp + 2q^2)h_0^3,$$

$$c_1(x,t) = -3h_0^2 h_{0,x}(G_\perp + q^2) + 3v - u,$$

$$c_0(x,t) = h_0^3 q^2(G_\perp + q^2) + 3v_x. \quad (10)$$

The freedom of choosing the value of u allows one to simplify the expressions in Eq. (10) in some particular cases. For instance, when the problem admits a traveling wave solution, there exists a particular value of u, say u^*, such that $h_{0,t}=0$. Thus, the coefficients in Eq. (10) become time independent, as for the CF flow [33]. On the other hand, when translational invariance is not allowed and no traveling wave solution exists, the coefficients are time dependent in any reference frame.

III. NUMERICAL METHOD

The stability analysis is performed by numerically solving the coupled system specified by Eqs. (4) and (6). The equations are discretized in space by centered finite differences and evolved in time by using a synchronized time marching Crank-Nicholson scheme. The solution of Eq. (4) is carried out by using an adjustable time increment Δt^n for the nth step, such that $t^{n+1}=t^n+\Delta t^n$. For further details of the numerical treatment of Eq. (4), we refer the reader to Ref. [44]. The synchronization between Eqs. (4) and (6) is done as follows: after $h_0(x,t^{n+1})$ has been evaluated using Eq. (4), we proceed to calculate $g(x,t^{n+1};\lambda)$ using Eq. (6). Within this time marching scheme, we calculate the coefficients c_i in Eq. (10) with interpolated values of the base state h_0 between t^n and t^{n+1}, since the time step for Eq. (6) is typically smaller than Δt^n for Eq. (4), due to convergence reasons.

The boundary conditions for Eq. (4) are $h_{0,x}=h_{0,xxx}=0$ and $h_0=h_0^*=$const at both ends of the domain, $x=0$ and $x=L$. The constant h_0^* depends on the problem at hand: it corresponds to the thickness far from the contact region in the CF flow, and to the precursor film thickness in the CV flow. For $g(x,t;\lambda)$ in Eq. (6) we use $g=g_x=g_{xxx}=0$ at $x=0$ and $x=L$.

The main difficulties in solving Eqs. (4)–(6) lay on the facts that the coefficients $c_i(x,t)$ ($i=0,\ldots,4$) are time dependent, and that they involve high derivatives of $h_0(x,t)$. Fortunately, the dependence on high derivatives can be written in terms of v and v_x [see Eqs. (10)]. Therefore, we can compute the velocity v by integrating the conservative form of Eq. (4), namely, Eq. (8), as

$$v = u + \frac{j - F}{h_0}, \quad (11)$$

where

$$F = \int_{x_0}^{x} h_{0,t}(x',t)dx' \quad (12)$$

is the rate of change of fluid volume within (x_0,x) at time t. Since the boundary conditions are time independent, the flux at $x=x_0$, $j=[v(x_0)-u]h_0(x_0)$, is a constant. Consistently, v_x is obtained from Eq. (8) as

$$v_x = -\frac{(v-u)h_{0,x} + h_{0,t}}{h_0}. \quad (13)$$

This method is employed in what follows to improve the accuracy of our scheme used to compute thin film flows.

A. Integral method applied to CF flow

In this section we compare the convergence of the velocity fields obtained by applying a standard centered finite difference scheme (CFDS) to Eq. (9) and from the integral

method, Eq. (11) in the CF flow. This flow corresponds to the spreading of a fluid film down an incline with fixed thickness h_* far behind the advancing front. The calculation of the traveling wave solution and its stability analysis is revisited in the Appendix, where we use a moving reference frame in which the solution is time independent. Here, we study the flow in the laboratory frame, with the goal of testing the numerical method in a time-dependent problem. As an initial condition we use a smoothed steplike function for the film profile which connects the "dry" region (covered by the precursor film of thickness h_f) and the bulk region. Due to the existence of a constant thickness bulk in the CF flow, it is convenient to choose the scales for this problem as

$$h_c = h_*, \quad x_c = \ell, \quad t_c = \tau, \tag{14}$$

where

$$\ell = \left(\frac{a^2 h_*}{\sin\alpha}\right)^{1/3}, \quad \tau = \frac{3\mu\,\ell^4}{\gamma h_*^3}. \tag{15}$$

With this choice of units, the dimensionless parameters in Eq. (2) become

$$G_\perp = \left(\frac{h_*}{a}\right)^{2/3} \frac{\sin^{1/3}\alpha}{\tan\alpha}, \quad G_\parallel = 1. \tag{16}$$

Thus, the boundary conditions are $h=1$, $h_x = h_{xxx} = 0$ at $x=0$, and $h=b$, $h_x = h_{xxx} = 0$ at $x=L$, where

$$b = \frac{h_f}{h_*}. \tag{17}$$

As shown in the Appendix, when the CF flow is considered in a moving reference frame with $u^* = 1 + b + b^2$, the height profile is time independent. Moreover, the expression for the velocity v can be simplified and written in terms of $h_0(x)$ [see Eq. (A8)]. In fact, that equation is a particular case of Eq. (11) with $F=0$, a result that will help us below to show the advantages of applying the proposed integral method.

Now we proceed to compare the velocity profiles in the vicinity of the front position, x_f, obtained using both approaches; that is, Eqs. (9) and (11). Figure 2 shows that as Δx is decreased, the difference between the solution obtained using the integral method and the exact solution [Eq. (A8)] decreases faster than for the solution calculated using the CFDS method. Therefore, we use the integral approach in what follows.

B. Validation of the numerical method applied to CF flow

Here we use CF flow as a benchmark for our computations. We check the consistency of the results for both the growth rate and shape of the perturbations in the laboratory frame by comparing the solutions of Eqs. (4) and (6) with those obtained in the moving reference frame. The latter approach is presented in the Appendix.

Figure 3(a) shows the evolution of a smoothed steplike initial condition. After a transient stage, a traveling wave profile develops. For long enough times, say $t=20$, Fig. 3(b) shows that the difference between this profile and the solution given in the Appendix (see Fig. 17) is at most 1.5%. This small difference suggests that the flow has reached a steady state. Then, we take the profile for $t > t_p = 20$ as the base solution on which we impose the perturbation. Here, we consider a perturbation of the form

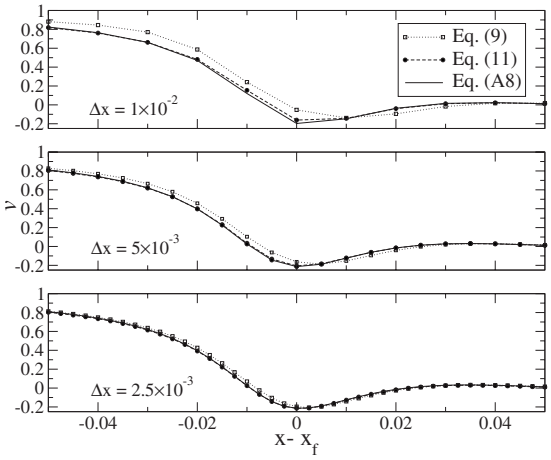

FIG. 2. Velocity profile $v(x,t=20)$ for the CF flow and $\alpha=90°$ in the laboratory frame ($u=0$). The results in the front region are shown for three different grid sizes, Δx. The open squares joined by the dotted lines correspond to the CFDS applied to Eq. (9), the filled squares joined with the dashed line correspond to the integral method, Eq. (11), and the solid line is the analytical solution, Eq. (A8). Here, the precursor thickness is $b=10^{-2}$.

$$g(x,t_p;\lambda) = \begin{cases} \sin\left[\pi \dfrac{x - x_r(t_p)}{x_f(t_p) - x_r(t_p)}\right], & x_r(t_p) < x < x_f(t_p) \\ 0, & \text{otherwise}, \end{cases} \tag{18}$$

where $x_r(t_p)$ and $x_f(t_p)$ are the ridge (maximum thickness) and the front positions at $t=t_p$, respectively. The motivation

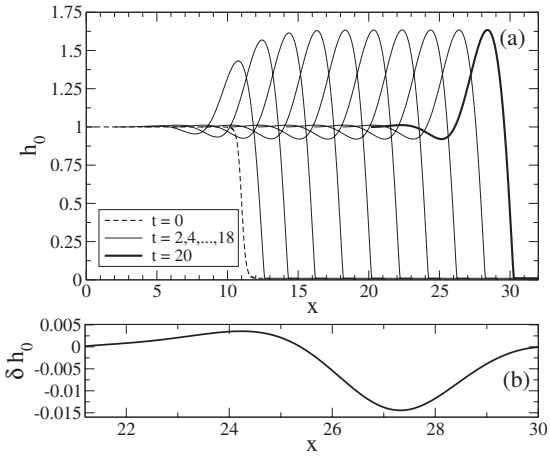

FIG. 3. (a) Evolution of the thickness profile $h_0(x,t)$ for $\alpha=90°$ for a smooth initial profile at $t=0$ for $b=10^{-2}$. (b) Difference δh_0 in the ridge region between $h_0(x,t=20)$ [thick line in (a)] and the thickness profile of the traveling wave of the CF flow shown in Fig. 17 of the Appendix.

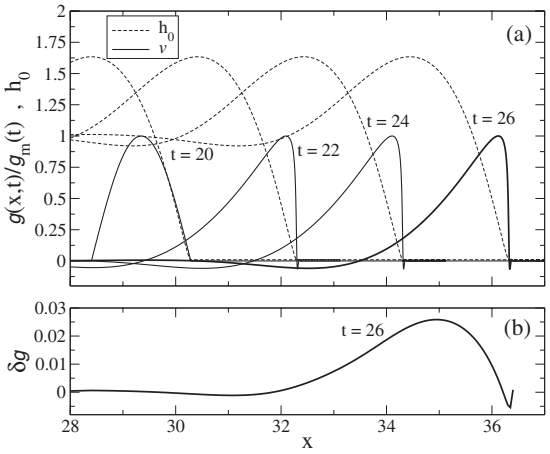

FIG. 4. (a) Evolution of a normalized perturbation $g(x,t;\lambda)/g_m(t;\lambda)$ for a vertical plane with $b=10^{-2}$ for $t \geq t_p=20$ and $\lambda=\lambda_m$ (solid lines). The dashed lines correspond to the simultaneous profiles of the base solution $h_0(x,t)$. (b) Difference δg in the ridge region between $g(x,t=26;\lambda)/g_m(t;\lambda)$ [thick line in (a)] and the eigenfunction calculated in the moving frame shown in Fig. 20(b) of the Appendix.

for concentrating the perturbation in this region is that it is the most sensitive zone to perturbations due to the presence of nonzero high order derivatives. Next, we calculate the evolution of this perturbation by solving Eq. (6), whose coefficients depend on the base solution $h_0(x,t)$. Note that this solution is time-dependent, since we work in the laboratory reference frame.

Figure 4(a) shows the evolution of the perturbation profile $g(x,t;\lambda)$ normalized with its maximum value $g_m(t)$ for $t > t_p$ and $\lambda=\lambda_m=12.56$, which corresponds to the maximum growth rate calculated in the Appendix. This normalized profile rapidly reaches a traveling wave form, and flows together with the base solution. Consequently, the perturbation does not spread, but it remains contained inside the front region [between $x_r(t)$ and $x_f(t)$]. For long times ($t \gg t_p$), one expects that the perturbation profile approaches the eigenfunction obtained by solving the eigenvalue problem (see Fig. 20 in the Appendix). Figure 4(b) shows that already for $t=26$ the difference between the two profiles is less than 7%. This result indicates that our computations correctly simulate the evolution of both the base flow and of the perturbation.

Figure 5 shows the time evolution of $g_m(t;\lambda)$ for three different wavelengths. This calculation can be carried out simultaneously for several λ's since their evolution is independent within the linear approximation. At early stages of the evolution, i.e., for times close to t_p, $g_m(t;\lambda)$ initially decreases. However, the magnitude of the perturbation, $g(x,t;\lambda)$, does not decrease everywhere in the domain. Figure 6 shows that even though $g_m(t;\lambda)$ decreases, $g(x,t;\lambda)$ increases close to the contact line.

For long times, Fig. 5 shows that $g_m(t;\lambda)$ approaches an exponential behavior. Here, we define the instantaneous growth rate for every mode as

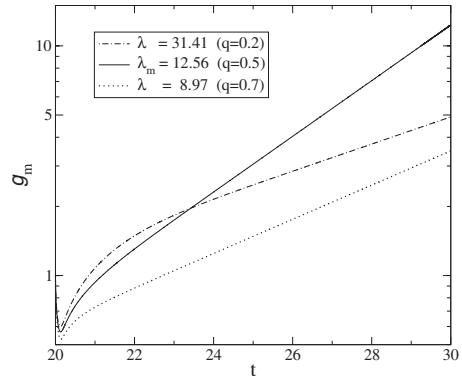

FIG. 5. Time evolution of the maximum of the perturbation amplitude $g_m(t;\lambda)$ for three different wavelengths ($q=2\pi/\lambda$ is the wave number) for $b=10^{-2}$. After an initial transient stage, $g_m(t;\lambda)$ grows exponentially as expected for the CF flow (semilogarithmic plot).

$$\sigma(t;\lambda) = \frac{1}{g_m}\frac{\partial g_m}{\partial t}. \tag{19}$$

Figure 7 shows the values of σ for very long times and several λ's. The successful comparison with the eigenvalues obtained in the Appendix supports the methodology used here. We also note that the same results (within numerical accuracy) are obtained in the co-moving reference frame translating with the velocity $u=u^*=1+b+b^2$.

Another check of our method is carried out by using an eigenfunction as the initial perturbation, instead of the one given by Eq. (18). In this case, we obtain exponential behavior of $g_m(t;\lambda)$ from the very beginning, with the growth rate as predicted by the corresponding eigenvalue.

IV. CONSTANT VOLUME FLOW

In this section we present the results for the flow of a constant volume (CV) of fluid. With the aim of presenting

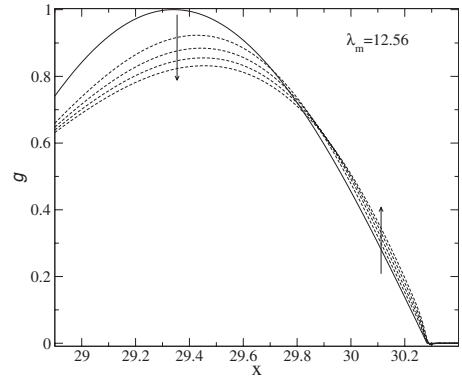

FIG. 6. Early evolution of the perturbation amplitude $g(x,t;\lambda)$ for $t=t_p+n\delta t$ with $n=0,1,\ldots,4$ and $\delta t=2\times10^{-3}$ (the arrows point in the direction of increasing t). Although $g(x,t;\lambda)$ decreases in the zone of its maximum, it increases in the region near the contact line [$x_f(t_p)=30.28$]. This effect explains the early decreasing region of $g_m(t;\lambda)$ in Fig. 5.

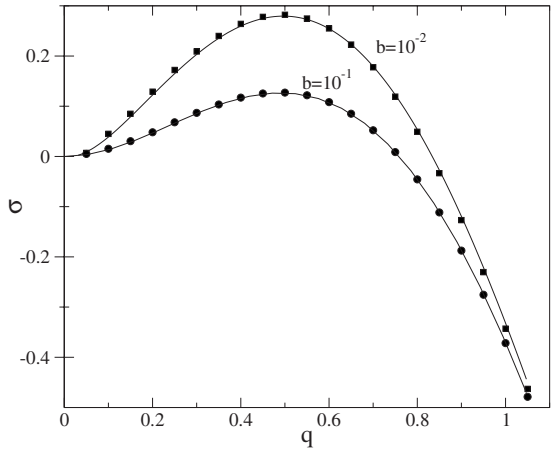

FIG. 7. Comparison of the asymptotic growth rates $\sigma(\infty;\lambda)$ defined by Eq. (19) (dots) and the eigenvalue curve (solid line) obtained in the Appendix.

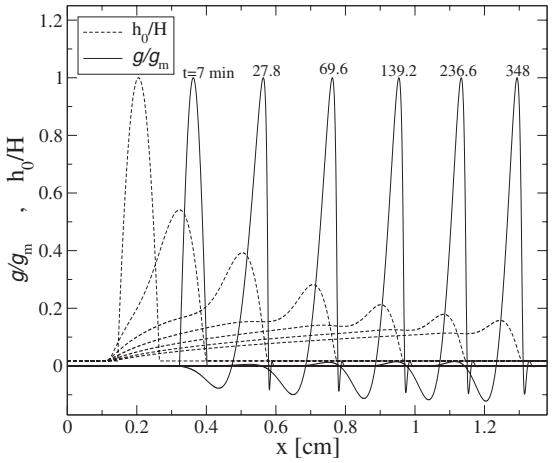

FIG. 8. Snapshots of the thickness (dashed lines) and perturbation (solid lines) profiles for the CV flow for $H=7.87\times10^{-3}$ cm and $w_0=0.1286$ cm ($\alpha=90°$). The base flow h_0 is shown for $t=0,7,27.8,69.6,139.2,236.6,348.0$ min. A perturbation characterized by $\lambda=0.49$ cm is imposed at $t_p=7$ min.

the main features of this flow and a simultaneous comparison with experimental data, we first consider as initial condition a fluid configuration closely resembling one of the experiments reported in Ref. [36], with $A=6.75\times10^{-4}$ cm^2 and width $w_0=0.1286$ cm. The present analysis allows one to give a more detailed description of the problem which is not accessible in the experiments, such as the spatial configuration and time evolution of the perturbations. Then, we also explore the influence of A and α on the wavelength of the mode of maximum amplitude, λ_{max}. For ease of comparison, in this section the results are presented in dimensional units.

It should be noted that any attempt to compare theoretical results with experiments involving a moving contact line, unavoidably requires the choice of an appropriate value of the small scale used to overcome the stress divergence at the contact line. In this respect, we showed in Ref. [36] that a *quantitative* description of the experimental thickness profile $h_0(x,t)$ requires one to use $h_f=3\times10^{-5}a$ for the precursor film model, where $a=0.145$ cm. With this value of h_f, numerical convergence is achieved for $\Delta x\leq10^{-3}a$. However, additional calculations show that accurate computations of $g(x,t;\lambda)$ [and consequently, of $\sigma(t;\lambda)$] require a grid step Δx of the same order as h_f even when the integral method for calculating velocities is used. This is due to the high accuracy needed in the evaluation of v and v_x for the coefficients c_i given by Eq. (10). Thus, comparison with experiments requires the use of both a small h_f and a typical domain of size $L\approx10a$,which leads to a number of grid points of the order of $N=10^5$. This large number results in long, time-consuming calculations even when carrying them out on up-to-date computers. As an example, evolving ten modes using $\Delta x=h_f=10^{-3}a$ (the values that we use in what follows) demands approximately three days of computing time on an Opteron 250 CPU. This choice of parameters yields reasonable computing times and accuracy. Clearly, with this value of h_f a *quantitative* comparison between experimental and numerical growth rates is not possible due to their strong dependence on h_f [33,34]. Nevertheless, we show below that the present analysis allows us to quantify other important features of the flow, such as λ_{max} and its dependence on A and α.

We point out that the onset time of the instability is not known *a priori*. Thus, the time at which perturbations are imposed in the simulations, t_p, is chosen to be less than the time at which undulations at the contact line are first observed in the experiments, t_0.

As a typical initial condition, we now take a cylindrical cap profile, which is consistent with small A's experiments [36,37]. It is defined by

$$h(x,0)=H[1-(x-x_0)^2/(w_0/2)^2], \tag{20}$$

where H is the maximum fluid height, x_0 is the position of the center of the cap, and w_0 is its initial width. Thus, the cross sectional area (in the x direction) is given by $A=2Hw_0/3$. The problem is solved in a large enough domain, $0\leq x\leq L$, so that the cap edges are far from the boundaries. The boundary conditions are similar to those used for the CF flow, except that here we keep the same value of h fixed at the boundaries, i.e., $h(0)=h(L)=h_f$.

We now compare the results of our calculations with experiments [36,37]. In the experimental setup, a horizontal filament of silicon oil [polydimethylsiloxane (PDMS) $\nu=\mu/\rho=20St$, $\rho=0.96$ g/cm^3, $\gamma=20$ dyn/cm] is placed on a vertical glass plate, so that the oil spreads down the plane by gravity under complete wetting conditions. The Bond number for this flow is very small, $B=(H/a)^2\approx3\times10^{-3}$.

Figure 8 shows the computational results for the evolution of h (dashed line) for the experimentally measured parameters $A=6.75\times10^{-4}$ cm^2 and $w_0=0.1286$ cm. For early times, this profile develops a ridge which includes a large fraction of the total fluid volume. For later times, both the height of the ridge and the amount of fluid in this region decrease, while its width remains fairly constant.

The stability study is carried out by perturbing the base state by a large set of modes (typically, 25) at $t_p=7$ min. We take the same initial amplitude for all modes and, since this particular value is irrelevant, we set it to unity. In Fig. 8 we

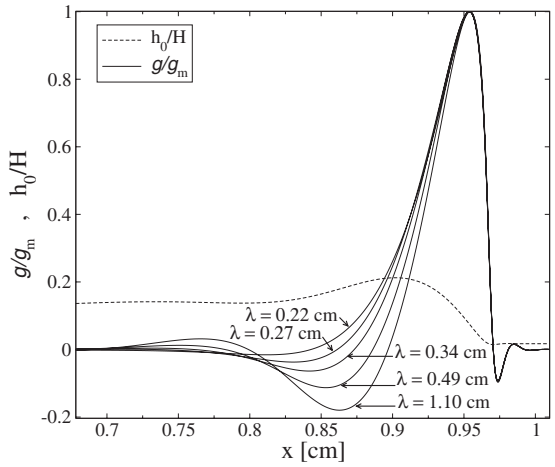

FIG. 9. Normalized perturbation profiles (solid lines) for $\lambda = 0.22, 0.27, 0.34, 0.49, 1.10$ cm at $t = 139.2$ min for the CV flow. The dashed line is the corresponding thickness profile $h_0(x, t = 139.2 \text{ min})$ (base flow) whose front is at $x_f = 0.97$ cm.

show the evolution of $g(x,t;\lambda)/g_m(t;\lambda)$ (solid line) for $t > t_p$ and $\lambda_{max} = 0.49$ cm, which corresponds to the mode of maximum amplitude (see below). Qualitatively similar profiles are obtained for other wavelengths. In spite of the fact that the base flow is time dependent, after a short transient stage, the normalized perturbation profile adopts an almost steady shape. We note that the perturbation moves together with the ridge, so that the peak remains contained between $x_r(t)$ and $x_f(t)$.

Figure 9 shows the perturbation shape for a number of wavelengths at $t = 139.2$ min. Note that all modes have the same shape near the contact line, but the amplitude far away from the front is larger for the longer wavelengths than for the shorter ones, showing that these longer wavelengths propagate deeper in the body of the fluid.

Figure 10 shows the amplitude spectra g_m vs λ. The wavelength of the maximum amplitude decreases with time, and finally reaches an asymptotic value $\lambda_{max} = 0.49$ cm, which is

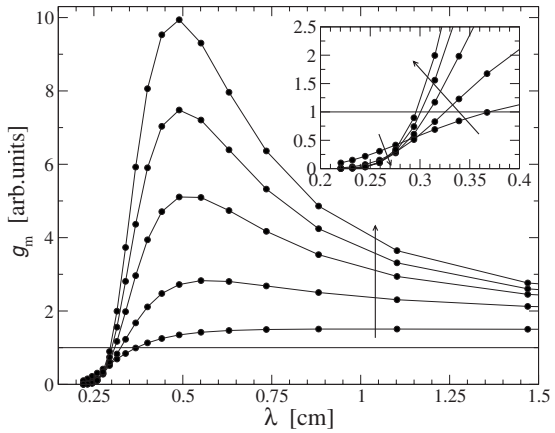

FIG. 10. Numerical spectra $g_m(t;\lambda)$ for $t = 20, 50, 100, 150, 200$ min (arbitrary units). The most unstable mode for long times has wavelength $\lambda_{max} = 0.49$ cm. The arrows indicate the direction of increasing time.

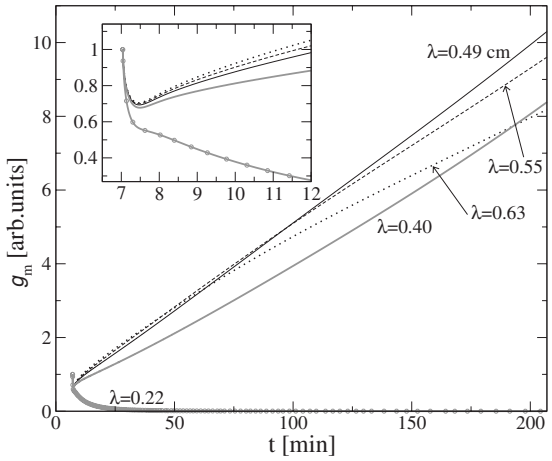

FIG. 11. Time evolution of the perturbation amplitudes for a set of modes in the CV flow. The linear behavior is similar to that of the experiment (see Fig. 12 below). The gray (black) lines correspond to $\lambda < \lambda_{max}$ ($\lambda > \lambda_{max}$), where $\lambda_{max} = 0.49$ cm. The inset shows a closeup of the evolution for early times.

reasonably close to the experimental value $\lambda_{max}^{expt} = 0.55$ cm of Ref. [36].

The inset of Figure 10 shows that there exists a narrow band of wavelengths $0.25 \text{ cm} < \lambda < 0.30$ cm, where the mode amplitudes remain practically constant. This band is the counterpart of the marginal stability mode in the CF flow.

Figure 11 shows the time evolution of $g_m(t;\lambda)$ for a set of λ's. We note that the amplitudes decrease within the first few seconds. This is due to an effect similar to the one shown in Fig. 6 for the CF flow [$g_m(t;\lambda)$ decreases although the perturbations' magnitude close to the contact line increases]. For later times, the amplitudes for short wavelengths ($\lambda \lesssim 0.25$ cm) decrease and, therefore, these modes are stable (see also Fig. 10). For long wavelengths ($\lambda \gtrsim 0.30$ cm), the amplitudes grow by following an approximately linear dependence with time, in agreement with the experimental data presented in Fig. 12. This is in contrast to the exponential growth in the CF flow, shown in Fig. 5. A more detailed

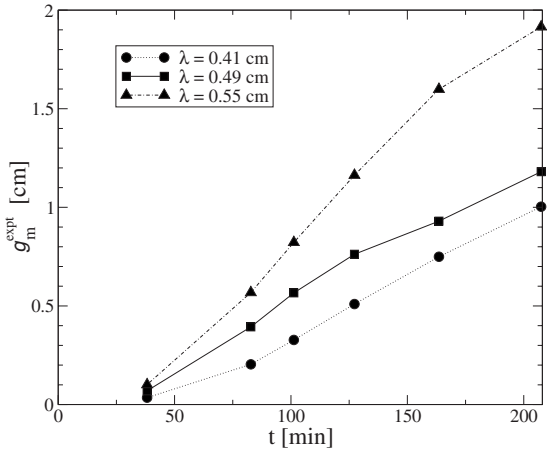

FIG. 12. Time evolution of three modal amplitudes g_m^{expt} from experiments [36].

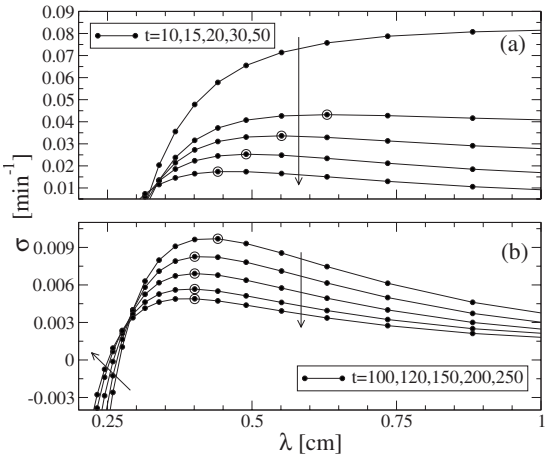

FIG. 13. Instantaneous growth rate of the perturbations as a function of λ in the CV flow. The maximum of the curves are encircled and the arrows indicate the direction of increasing time.

comparison between Figs. 11 and 12 shows that the numerical growth is smaller than the experimental ones. This is due to the discrepancy in the precursor film thickness, as discussed earlier. For example, Fig. 12 shows that the experimental amplitude corresponding to $\lambda=0.55$ cm grows 18.9 times in the interval $(t_0, 207$ min), while the numerical one increases only by a factor of 4.2. Here $t_0=38.2$ min is the time when we first observe undulations of the contact line in the experiments[36].

Figure 13 shows the instantaneous growth rate $\sigma(t;\lambda)$ [see Eq. (19)], as a function of λ for different times. The main observation is that the absolute values of all growth rates decrease with time. For early times shown in Fig. 13(a), the wavelength of maximum instantaneous growth rate rapidly decreases with time. For example, at $t=15$ min, the largest σ corresponds to $\lambda=0.60$ cm, while at $t=20$ min it corresponds to $\lambda=0.55$ cm. From $t=100-250$ min, the maximum of these curves corresponds to $\lambda=0.40$ cm [see Fig. 13(b)]. Nevertheless, the growth rate of this mode is not large enough to dominate the amplitude spectra, since, as shown in Fig. 10, the mode with largest amplitude corresponds to 0.49 cm. This is possible since the mode amplitude is proportional to the integrated growth $\exp[\int\sigma(t;\lambda)dt]$, and not merely to $\exp[\sigma t]$, as for a time-independent base solution. We also note that Fig. 13(b) suggests the existence of a mode with $\lambda\approx0.29$ cm whose growth rate remains constant, in this case with $\sigma\approx3.1\times10^{-3}$. Consequently, this mode is the only one characterized by pure exponential growth. Additional simulations show that this constant growth rate depends on the value of h_f: it decreases for larger h_f and could even become negative for a sufficiently thick precursor.

A more detailed analysis can be carried out by comparing the numerical and experimental power spectra. The latter are obtained by calculating the Fourier transform of the shape of the contact line [36]. Here, we predict the evolution of an early experimental spectrum $I(t_0;\lambda)$ and compare this prediction with the spectra observed in experiments at several times $t>t_0$. To proceed, we first define the auxiliary amplitude,

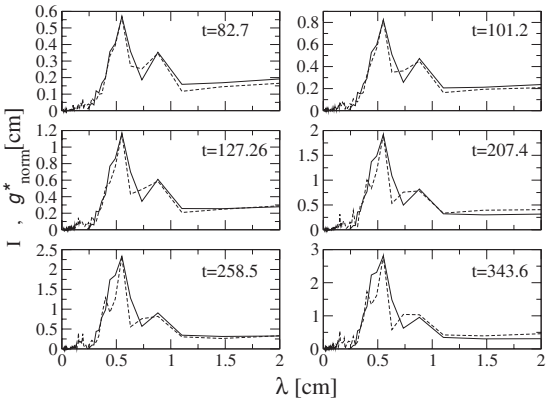

FIG. 14. Comparison between the experimental spectra $I(t;\lambda)$ (dashed line) and the normalized numerical spectra $g^*_{norm}(t;\lambda)$ (solid line) calculated using Eq. (22).

$$g^*(t;\lambda)=g_m(t;\lambda)\frac{I(t_0;\lambda)}{g_m(t_0;\lambda)}, \tag{21}$$

where $g_m(t;\lambda)$ is shown in Fig. 10. Thus, $g^*(t;\lambda)$ corresponds to the initial spectrum $I(t_0;\lambda)$ at $t=t_0$. Since, as mentioned above, the use of a relatively large value of h_f yields lower growth rates than the experiments, the spectrum $g^*(t;\lambda)$ cannot quantitatively predict the values of experimental amplitudes. Nevertheless, it is possible to compare the *shapes* of the spectra for different times by normalizing $g^*(t;\lambda)$ with the peak value of the experimental ones at that time, in the form

$$g^*_{norm}(t;\lambda)=g^*(t;\lambda)\frac{I(t;\lambda^{expt}_{max})}{g^*(t;\lambda^{expt}_{max})}, \tag{22}$$

where $g^*_{norm}(t;\lambda)$ is the normalized predicted spectra. Figure 14 shows that a general good agreement between $g^*_{norm}(t;\lambda)$ and the experimental spectra $I(t;\lambda)$ is found. Since the normalization is done by using the maximum amplitude of a single wavelength λ^{expt}_{max}, the good agreement for all other wavelengths implies that the only difference between the predicted spectra and the experimental ones can be reduced to a single scaling function. Therefore, we can assume that $I(t;\lambda)\approx g^*_{norm}(t;\lambda)$, and Eq. (22) can be rewritten as

$$\frac{g^*(t;\lambda)}{I(t;\lambda)}\approx\frac{g^*(t;\lambda^{expt}_{max})}{I(t;\lambda^{expt}_{max})}, \tag{23}$$

which implies that the ratio between numerical and experimental amplitudes g^*/I is independent of λ and it is only a function of time.

A. Dependence of λ_{max} on A and α

Here we discuss how the wavelength of maximum amplitude λ_{max} varies with the cross sectional area A, and the inclination angle α. Figure 15 shows the results for two different inclination angles $\alpha=90°$ (lower line) and 45° (upper line), in a range of A's similar to that of the experiments in Ref. [37]. The error bars are due to the fact that the ampli-

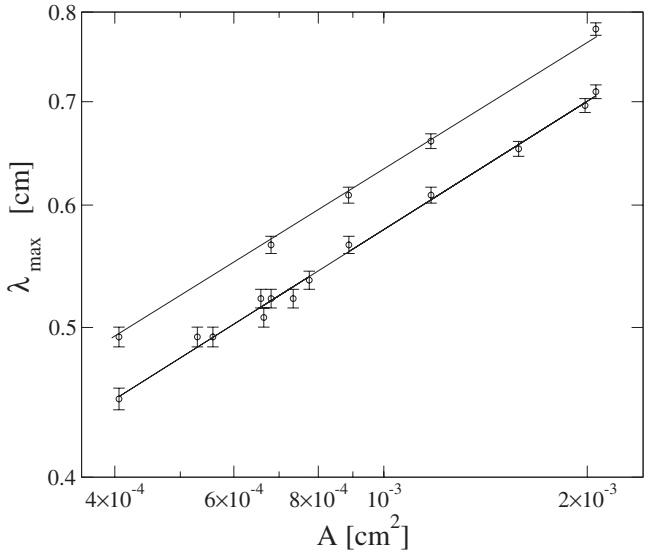

FIG. 15. Dependence of the most unstable mode λ_{max} on the cross section A for $\alpha=45°$ (upper set of points) and $\alpha=90°$ (lower set of points).

tude spectra are calculated for a set of discrete values of λ. For $\alpha=90°$ we find

$$\lambda_{max} \propto A^{0.27},$$

in excellent agreement with the experimental results [37]. This dependence is also very close to that proposed in Ref. [38], i.e., $\lambda_{max} \propto A^{0.25}$. For $\alpha=45°$, the simulations show that the power law dependence has basically the same exponent, as suggested by the upper line in Fig. 15. The fact that the exponent does not change with α implies that the component of gravity perpendicular to the plane does not influence λ_{max}. However, as expected, this force does affect the growth rates of the unstable modes.

Figure 16 shows the dependence of λ_{max} on α, for two different A's and $5° \leq \alpha \leq 90°$. We find

$$\lambda_{max} \propto (\sin \alpha)^{-0.247},$$

with an exponent close to that obtained by the dimensional analysis reported in Ref. [37].

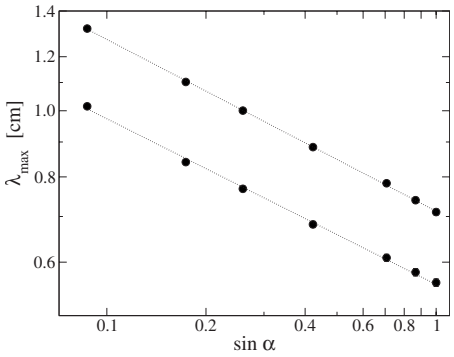

FIG. 16. Dependence of λ_{max} on the inclination angle α for $A=2.06\times10^{-3}$ cm^2 (upper set of points) and $A=0.90\times10^{-3}$ cm^2 (lower set of points).

V. CONCLUSIONS

We study the linear stability of the contact line for a constant volume (CV) of fluid spreading down an incline, as an example of a flow with no translational invariance. In contrast to constant flux (CF) flow, the base state is time dependent, as it occurs in most of the flows found in applications. The analysis presented here avoids the use of simplified conditions, such as the imposition of a constant fluid thickness in the bulk region, and aims to give a more accurate description of the instability in realistic flows.

One hindrance found when solving the linear equation that governs the evolution of the perturbations, namely, Eq. (6), is the accuracy needed to evaluate its coefficients. We use here an integral method, Eq. (11), to improve the accuracy of the fluid velocities' computations. One of the merits of the proposed method is its simplicity and ease of adapting to other flow configurations.

For the CV flow, a normalized perturbation travels with the same velocity as the front and, after a short transient period, it adopts an asymptotic final shape. Regarding the amplitude of the perturbation, we find that it grows approximately linearly with time, unlike the CF flow where the growth is exponential.

The study of the evolution of the power spectrum $g_m(t;\lambda)$ and the growth rate $\sigma(t;\lambda)$, shows some interesting features of the dynamics of the perturbation. For instance, the wavelength corresponding to the mode of maximum amplitude is time dependent, unlike in the CF flow, and it decreases until an asymptotic value is reached. Moreover, for a given time, the growth rate of this wavelength is not necessarily the largest. This is possible since the instantaneous value of $\sigma(t;\lambda)$ depends on time, and then, the amplitude of each mode for the CV flow is given by the time integral $\exp[\int \sigma(t;\lambda)dt]$. For example, Figs. 10 and 13 show that for $t=200$ min, the mode with $\lambda=0.49$ cm corresponds to the maximum amplitude, but the maximum instantaneous growth rate corresponds to $\lambda=0.40$ cm.

When the same initial amplitude is assigned to all the modes, the dominant wavelength λ_{max} is in good agreement with the experimental one. In the typical case studied here, we estimate $\lambda_{max}=0.49$ cm, which is reasonably close to the experimental value $\lambda_{max}^{expt}=0.55$ cm. The difference between these wavelengths is due to the fact that in experiments the initial amplitudes of the modes are not necessarily equal to each other, as we set in the simulations. The agreement between these wavelengths is complete when experimental amplitudes (at some early time) are used as input in the computations, as shown in Fig. 14.

The present method gives a better estimate of λ_{max} than those obtained by using a matching thickness to apply the CF solution to the CV flow. For example, recalling that the dominant wavelength of the CF flow is $\lambda_m=12.56\ell$ and taking H as a characteristic thickness of CV flow, i.e., $h_*=H$ $(=7.87\times10^{-3}$ cm), the predicted wavelength is $\lambda_{max}=0.69$ cm, further away from the experimental result $\lambda_{max}^{expt}=0.55$ cm. A good agreement requires one to set $h_*=0.51H$. However, there is no *a priori* reason for this choice of h_*.

In order to carry out simulations with reasonable use of computing resources, the calculations of the perturbation

evolution are carried out using the values of a precursor film thickness h_f larger than the real ones. Therefore, a quantitative comparison between calculated and experimental growth rates is not possible due to different viscous dissipation rates at the contact line region. Nevertheless, we find a very good agreement between the shape of the power spectra even for later times of the evolution. This suggests that the only difference between experimental and numerical spectra is a function of time, which only depends on the value of h_f.

The study of the dependence of the most unstable wavelength λ_{max} on the cross sectional area A confirms the power law dependence found in previous works for inclination angle $\alpha=90°$ [37,38]. Moreover, here we show that this dependence is still valid for $\alpha<90°$, with the same exponent. We also study the effect of α on λ_{max} ($5° \leq \alpha \leq 90°$), and conclude that a relationship of the type

$$\lambda_{max} \propto A^{0.27}/(\sin \alpha)^{0.247} \tag{24}$$

holds for the range of A's explored in this work, that is, $A \ll 1$ cm^2, corresponding also to Bond numbers $B \ll 1$. To our knowledge, this is the first time that this dependence has been explicitly determined for inclination angles different than 90°. This result confirms the predictions based on dimensional analysis in Ref. [37]. We point out that the dependence of λ_{max} on A is significantly different from the one reported for much larger cross section areas (and correspondingly, large Bond numbers) [12]. Therefore, the study presented here constitutes an example where the knowledge of large scale physics cannot be directly applied to micrometric flows.

ACKNOWLEDGMENTS

J.G. acknowledges the NSF Grant No. 0122911 that supported his visit to NJIT. He also thanks the Department of Mathematical Sciences of NJIT for hospitality. J.G., J.D., R.G., and A.G.G. acknowledge support from Agencia Nacional de Promoción Científica y Tecnológica (ANPCyT, Argentina) and CONICET.

APPENDIX: CONSTANT FLUX FLOW

Here we give an overview of linear stability analysis in a moving reference frame, where the base solution is stationary. We use the results obtained here to compare with the computational results of the same problem obtained in the laboratory frame.

In order to find a stationary solution in a moving reference frame, we consider $\partial h/\partial t=0$ in Eq. (4) with the scaling defined by Eqs. (14)–(17). Then, the first integral of this equation is written as

$$h_0^3 h_{0,xxx} + h_0^3 - G_\perp h_0^3 h_{0,x} - u^* h_0 = j, \tag{A1}$$

where $h_0(x)$ is the traveling wave solution, and j is an integration constant. Here, u^* is the speed of the particular moving reference frame in which the shape of the thickness profile is frozen, i.e., the phase velocity of the wave.

By applying the boundary conditions

$$h_0(-\infty)=1, \quad h_0(\infty)=b, \tag{A2}$$

we find

$$u^* = 1 + b + b^2, \quad j = -b(1+b). \tag{A3}$$

Equation (A1) is a third order ordinary differential equation that can be integrated by using a standard shooting method in a finite domain which spans from the plateau region where $h_0 \approx 1$, to the precursor film zone ($h_0 \approx b$). For a region far away from the contact line, the fluid thickness can be approximated by

$$h_0(x \to -\infty) = 1 + \xi(x), \tag{A4}$$

where $\xi(x)$ is a small quantity. Replacing this expression in Eq. (A1) and keeping only the first order terms, we obtain the following equation for ξ:

$$\xi_{xxx} = G_\perp \xi_x - b(b+1)(1-3\xi) + (1+b+b^2)(1-2\xi) - 1.$$

The solution of this equation has the form $\xi_0 e^{\beta x}$, where ξ_0 is an unknown constant and the complex exponent β satisfies

$$\beta^3 = G_\perp \beta - C, \tag{A5}$$

with $C=2-b-b^2$. Taking the real part of the solution and disregarding terms with exponentials which diverge for $x \to -\infty$, we finally obtain

$$h_0(x \to -\infty) = 1 + \xi_0 \exp(\beta_1 x)\cos(\beta_2 x), \tag{A6}$$

where

$$\beta_1 = \frac{6G_\perp + 2^{1/3}(27C + \sqrt{729C^2 - 108G_\perp^3})^{2/3}}{6 \times 2^{2/3}(27C + \sqrt{729C^2 - 108G_\perp^3})^{1/3}},$$

$$\beta_2 = \sqrt{3}\frac{6D - 2^{1/3}(27C + \sqrt{729C^2 - 108G_\perp^3})^{2/3}}{6 \times 2^{2/3}(27C + \sqrt{729C^2 - 108G_\perp^3})^{1/3}}. \tag{A7}$$

Equation (A6) allows one to obtain the first and second derivatives far away from the contact line, which are necessary to apply the shooting method to solve Eq. (A1). We proceed by setting a seed value for the constant ξ_0 and integrating forward in the direction of increasing x. We iteratively modify the value of ξ_0 until h_0 approaches b (beyond the contact line region) within a given tolerance. This procedure, performed under Mathematica©, demands a computing time of a few minutes for $b=0.01$.

Figure 17 shows the thickness profile as obtained with the above procedure for two values of b on a vertical substrate ($G_\perp=0$). The origin of the x coordinate is chosen to coincide with the position of the minimum of h_0. The inset shows a closeup of the contact line zone, where an oscillatory structure develops. Additional calculations show that the typical length of this structure diminishes with the thickness of the precursor film b. Figure 18 shows that the maximum height $h_{0,max}$ increases logarithmically when b decreases.

A useful property of this traveling wave solution is that the flow velocity v can be expressed by a very simple form which depends on the thickness profile $h_0(x)$, but not on its derivatives. This fact makes this variable suitable to validate the calculation of v based on the integral method described

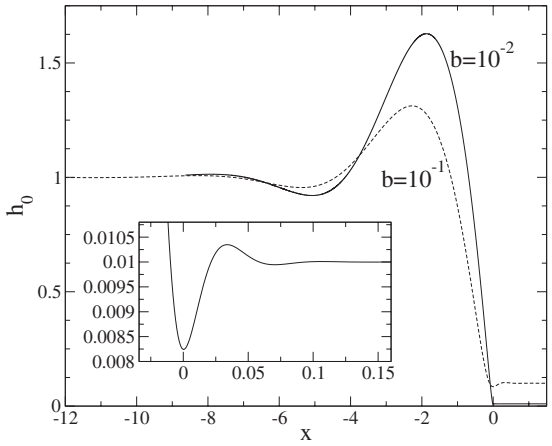

FIG. 17. Thickness profiles obtained by integrating Eq. (A1) for $G_\perp=0$ with $b=10^{-1}$ and $b=10^{-2}$. The inset shows the oscillation of the film thickness in the contact line zone for $b=10^{-2}$.

in Sec. III. By replacing $h_{0,xxx}$ from Eq. (A1), we obtain [see Eq. (9)]

$$v(x) = u^* + \frac{j}{h_0(x)}. \tag{A8}$$

Since the flux j is negative, Eq. (A8) indicates that the maximum (minimum) of h_0 occurs at the same position as the maximum (minimum) of v. Figure 19 shows the velocity profiles (solid lines) for two values of b, as obtained from Eq. (A8) by using the thickness profiles $h_0(x)$ (dashed lines). Interestingly, due to the region of negative v's in the contact line zone, a given fluid element in the precursor film, which is reached by the advancing traveling wave is first "sucked" toward the bulk region and then accelerated forward.

1. Linear Stability Analysis

In order to perform a linear stability analysis of the traveling wave solution $h_0(x)$, with respect to perturbations in the transverse direction y, we write

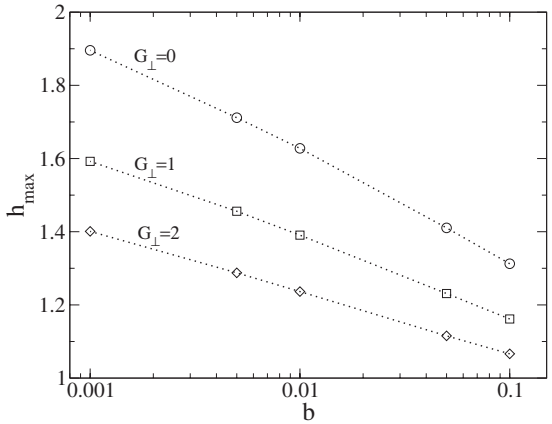

FIG. 18. Height of the bump $h_{0,max}$ as a function of b for three values of $G_\perp$.

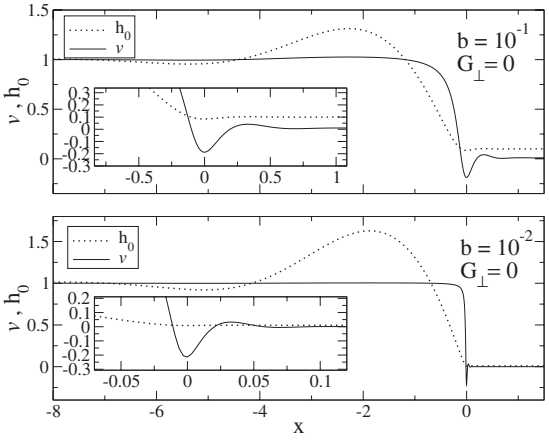

FIG. 19. Velocity v (solid line) for $b=10^{-1}$ and 10^{-2}. The dotted line is the thickness profile. The insets shows a zoom of the contact line zone.

$$h(x,y,t) = h_0(x) + \epsilon g(x)\exp(\sigma t)\exp(iqy), \tag{A9}$$

where ϵ is a small number, σ is the growth rate, $q=2\pi/\lambda$ is the wave number, and λ is the wavelength of the perturbation. By replacing Eq. (A9) in Eq. (1), and considering Eq. (16), we obtain

$$\mathcal{L}g = -\sigma g, \tag{A10}$$

where $\mathcal{L}$ is a linear operator defined by

$$\mathcal{L} \equiv c_4(x)\frac{d^4}{dx^4} + c_3(x)\frac{d^3}{dx^3} + c_2(x)\frac{d^2}{dx^2} + c_1(x)\frac{d}{dx} + c_0(x). \tag{A11}$$

The coefficients $c_i(x)$, with $i=0,\ldots,4$, depend on h_0 and its derivatives in the form

$$c_4(x) = h_0^3,$$

$$c_3(x) = 3h_0^2 h_{0,x},$$

$$c_2(x) = -h_0^3(2q^2 + G_\perp),$$

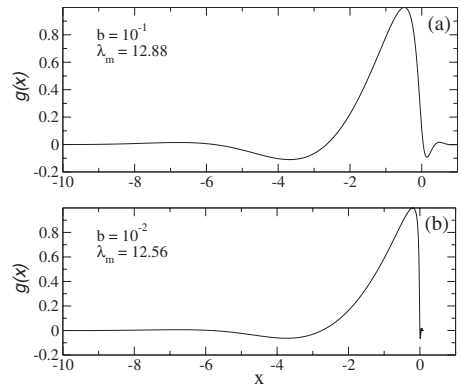

FIG. 20. Eigenfunctions for a spreading on a vertical plane ($G_\perp=0$): (a) $b=10^{-1}$, (b) $b=10^{-2}$.

$$c_1(x) = 3j/h_0 + 2u^* - 3h_0^2 h_{0,x}(q^2 + G_\perp),$$

$$c_0(x) = -3jh_{0,x}/h_0^2 + h_0^3 q^2(q^2 + G_\perp). \quad \text{(A12)}$$

These equations are a modified version of Eq. (10) for a reference frame moving at velocity u^* as given by Eq. (A3) (note that here h_0 is time independent).

The eigenvalue problem given by Eq. (A10) is solved numerically by using the algorithms in the package EISPACK within the same domain in which $h_0(x)$ is previously calculated. Figure 7 shows the result, together with the output of the computations carried out in the laboratory frame. We find that for the flow down a vertical plane ($G_\perp = 0$) and for both considered b's, $b = 10^{-1}$ and 10^{-2}, the wavelength of maximum growth is $\lambda_m = 2\pi/q_m = 12.88$ and 12.56, respectively. Figure 20 shows the eigenfunctions for λ_m and the same set of b's. For smaller b, the leading edge at $x = 0$ is steeper and the region of the frontal dip is more narrow.

[1] H. A. Stone, A. D. Stroock, and A. Ajdari, Annu. Rev. Fluid Mech. **36**, 381 (2004).
[2] C. H. Ho and Y. C. Tai, Annu. Rev. Fluid Mech. **30**, 579 (1998).
[3] M. Freemantle, Chem. Eng. News **77**, 27 (1999).
[4] D. E. Kataoka and S. M. Troian, Nature (London) **402**, 794 (1999).
[5] W. Menz and A. Guber, Minim Invasive Neurosurg. **37**, 21 (1994).
[6] A. A. Darhuber and S. M. Troian, Annu. Rev. Fluid Mech. **37**, 425 (2005).
[7] Y. Pomeau and E. Villermaux, Phys. Today **59**, 39 (2006).
[8] P. G. de Gennes, Rev. Mod. Phys. **57**, 827 (1985).
[9] E. B. Dussan, E. Rame, and S. Garoff, J. Fluid Mech. **230**, 97 (1991).
[10] J. B. Keller and M. J. Miksis, SIAM J. Appl. Math. **43**, 268 (1983).
[11] A. Oron, S. H. Davis, and S. G. Bankoff, Rev. Mod. Phys. **69**, 931 (1997).
[12] H. Huppert, Nature (London) **300**, 427 (1982).
[13] L. M. Hocking, W. R. Debler, and K. E. Cook, Phys. Fluids **11**, 307 (1999).
[14] J. R. deBruyn, Phys. Rev. A **46**, R4500 (1992).
[15] S. M. Troian, X. L. Wu, and S. A. Safran, Phys. Rev. Lett. **62**, 1496 (1989).
[16] E. Ramos de Souza and D. Gallez, Phys. Fluids **10**, 1804 (1998).
[17] O. E. Jensen and J. B. Grotberg, J. Fluid Mech. **240**, 259 (1992).
[18] N. Fraysse and G. M. Homsy, Phys. Fluids **6**, 1491 (1994).
[19] F. Melo, J. F. Joanny, and S. Fauve, Phys. Rev. Lett. **63**, 1958 (1989).
[20] J. A. Moriarty, L. W. Schwartz, and E. O. Tuck, Phys. Fluids A **3**, 733 (1991).
[21] I. S. McKinley and S. K. Wilson, Phys. Fluids **14**, 133 (2002).
[22] L. W. Schwartz and R. Valery Roy, Phys. Fluids **16**, 569 (2004).
[23] P. Carles, S. M. Troian, A. M. Cazabat, and F. Heslot, J. Phys.: Condens. Matter **2**, SA477 (1990).
[24] M. J. Tan, S. G. Bankoff, and S. H. Davis, Phys. Fluids A **2**, 313 (1990).
[25] M. L. Ford and A. Nadim, Phys. Fluids **6**, 3183 (1994).
[26] X. Fanton, A. M. Cazabat, and D. Quéré, Langmuir **12**, 5875 (1996).
[27] D. E. Kataoka and S. M. Troian, J. Colloid Interface Sci. **192**, 350 (1997).
[28] D. E. Kataoka and S. M. Troian, J. Colloid Interface Sci. **203**, 335 (1998).
[29] S. W. Benintendi and M. K. Smith, Phys. Fluids **11**, 982 (1999).
[30] N. Silvi and E. B. Dussan V, Phys. Fluids **28**, 5 (1985).
[31] J. M. Jerrett and J. R. deBruyn, Phys. Fluids A **4**, 234 (1992).
[32] Y. Ye and H. Chang, Phys. Fluids **11**, 2494 (1999).
[33] A. L. Bertozzi and M. P. Brenner, Phys. Fluids **9**, 530 (1997).
[34] S. M. Troian, E. Herbolzheimer, S. A. Safran, and J. F. Joanny, Europhys. Lett. **10**, 25 (1989).
[35] J. A. Diez, L. Kondic, and A. Bertozzi, Phys. Rev. E **63**, 011208 (2000).
[36] A. G. González, J. Diez, J. Gomba, R. Gratton, and L. Kondic, Phys. Rev. E **70**, 026309 (2004).
[37] J. Gomba, J. Diez, A. G. González, and R. Gratton, Phys. Rev. E **71**, 016304 (2005).
[38] L. W. Schwartz, Phys. Fluids A **1**, 443 (1989).
[39] I. Veretennikov, A. Indekina, and H. Chang, J. Fluid Mech. **373**, 81 (1998).
[40] B. M. Marino, L. P. Thomas, J. A. Diez, and R. Gratton, J. Colloid Interface Sci. **177**, 14 (1996).
[41] E. B. Dussan V, Annu. Rev. Fluid Mech. **11**, 317 (1979).
[42] V. Ludviksson and E. N. Lightfoot, AIChE J. **14**, 674 (1968).
[43] R. J. Hansen and T. Y. Toong, J. Colloid Interface Sci. **36**, 410 (1971).
[44] J. Diez and L. Kondic, J. Comput. Phys. **183**, 274 (2002).